Received: 10 July 2023 | Revised: 12 October 2023 | Accepted: 24 October 2023

DOI: 10.1002/mawe.202300161

ARTICLE

WILEY VCH

Ray tracing method with implicit surface detection for smoothed particle hydrodynamics-based laser beam welding simulations

Strahlverfolgungsmethode mit impliziter Oberflächenerkennung für geglättete Partikel durch hydrodynamisch-basierte Laserstrahlschweißsimulationen

L. Westhofen[1] | **J. Kruska**[2] | **J. Bender**[1] | **S. Warkentin**[2] | **O. Mokrov**[2] | **R. Sharma**[2] | **U. Reisgen**[2]

[1]RWTH Aachen University, Visual Computing Institute, Aachen, Germany

[2]RWTH Aachen University, Welding and Joining Institute, Aachen, Germany

Correspondence
L. Westhofen, RWTH Aachen University, Visual Computing Institute, Ahornstraße 55, 52056, Aachen, Germany.
Email: l.westhofen@informatik.rwth-aachen.de

Funding information
RWTH Aachen University, Grant/Award Number: SFB1120-236616214; Deutsche Forschungsgemeinschaft e. V. (DFG, German Research Foundation)

Abstract

An important prerequisite for process simulations of laser beam welding is the accurate depiction of the surface energy distribution. This requires capturing the optical effects of the laser beam occurring at the free surface. In this work, a novel optics ray tracing scheme is proposed which can handle the reflection and absorption dynamics associated with laser beam welding. Showcasing the applicability of the approach, it is coupled with a novel surface detection algorithm based on smoothed particle hydrodynamics (SPH), which offers significant performance benefits over reconstruction-based methods. The results are compared to state-of-the-art experimental results in laser beam welding, for which an excellent correspondence in the case of the energy distributions inside capillaries is shown.

KEYWORDS
heat transfer, hydrodynamics, laser beam welding, ray optics, ray tracing, smoothed particle

Abstract

Eine wichtige Voraussetzung für die Prozesssimulationen des Laserstrahlschweißens ist die genaue Darstellung der Oberflächenenergieverteilung. Dies erfordert die Erfassung der optischen Effekte des Laserstrahls, die an der freien Oberfläche auftreten. In dieser Arbeit wird ein neuartiges optisches Strahlverfolgungsverfahren vorgeschlagen, das die Reflexions- und Absorptionsdynamik beim Laserstrahlschweißen erfassen kann. Um die Anwendbarkeit des Ansatzes zu demonstrieren, wird dieser mit einem neuartigen Algorithmus zur Oberflächendetektion gekoppelt, der auf geglättete Partikel

hydrodynamisch (SPH) basiert und erhebliche Laufzeitvorteile gegenüber rekonstruktionsbasierten Methoden bietet. Die Ergebnisse werden mit den experimentellen Ergebnissen aus der aktuellen Forschung des Laserstrahlschweißens verglichen, für die eine ausgezeichnete Übereinstimmung im Fall der Energieverteilungen in Kapillaren gezeigt wird.

SCHLÜSSELWÖRTER
geglättete Partikel, hydrodynamische, Laserstrahlschweißen, Strahloptik, Strahlverfolgung, Wärmetransfer

1 | INTRODUCTION

Laser beam welding is a highly complex process influenced by the fluid dynamics of the melt pool, melting and solidification, and evaporation. A full process simulation of laser beam welding requires treating heat transfer, mass transfer and the energy transfer of the laser beam through reflection and refraction. Note that the former two are mainly driven by the latter. Since the simulation geometry is undergoing constant changes through the dynamics of the welding process, coupling the simulation of the energy distribution to the heat and mass transfer becomes essential for highly accurate results.

State-of-the-art solutions employ a ray tracing scheme to model the optical phenomena like reflection and refraction of the incident laser [1–5]. Since this model is close to the real-world properties of propagating light rays, it is particularly well suited to capture the underlying ray optics and thus the energy distribution given by the laser as the primary heat source. Thus, this work follows this approach by employing a ray tracing scheme as well.

For the subsequent process simulation, smoothed particle hydrodynamics has been shown to be well applicable to the simulations of heat and mass transfer needed in welding engineering [6–11]. Due to the meshless, Lagrangian nature of smoothed particle hydrodynamics, it conserves mass by construction and eases the treatment of topological changes. Thus, a process simulation using smoothed particle hydrodynamics is envisioned to be the goal, which necessitates a surface depiction for the seamless energy transfer of the laser to the heat simulation.

In this work, a novel smoothed particle hydrodynamics surface handling approach which can be easily coupled with a ray tracing scheme is presented. The model is entirely smoothed particle hydrodynamics-based, which eliminates the need for expensive, explicit surface tracking or reconstruction. Additionally, a possible implementation of a sphere tracing algorithm for the implementation of ray tracing is also provided, coupling it with the surface handling scheme using an upper-bound distance estimator. This model then serves as the basis for a qualitative analysis for both synthetic scenarios and the case study of the energy density inside welding capillaries formed by laser beam welding in which results obtained by x-ray imaging are compared against state-of-the-art results [12]. A good agreement with the expected results will be demonstrated, both qualitatively and quantitatively. Thus, a surface handling and subsequent ray tracing approach well-suited for smoothed particle hydrodynamics-based laser beam welding simulation is proposed and lays an important foundation for future process simulations.

2 | RELATED WORK

This work is concerned with laser beam welding. The whole process encompasses the complex interplay between energy absorption, metal evaporation and the fluid dynamics of the melt pool around the capillaries formed. Since small parameter changes may have a large impact on the welding results, simulations for cheap and non-destructive insights become particularly interesting.

There have been many models proposed for the simulation of laser beam welding [2, 3, 13, 14]. Capturing the interaction of the laser as the primary heat source with the work piece and the weld pool is of utmost importance. Since the laser is a source of coherent electromagnetic radiation, one approach is to solve Maxwell's equations with for example a two-dimensional, axial-symmetric approach based on the finite element method [5]. However, solving the full set of Maxwell's equations requires a lot of computational effort. Another approach is ray tracing, which offers to capture the desired properties of the laser at the appropriate scale for a fraction of the cost. In recent state-of-the-art publications, this has been coupled with a volume-of-fluid method and an octree representation to efficiently capture many laser applications like welding or cutting [2]. Concerning smoothed particle hydrodynamics as the simulation method for the thermodynamics and hydrodynamics of

the melt pool, there have been multiple methods have been proposed [1, 3, 4]. For coupling, one approach is to reconstruct the surface mesh from the narrow band of surface particles and compute the ray tracer interactions using ray-triangle intersections [3, 4]. However, this has the disadvantage of requiring a lot of additional computational overhead since any reconstruction-based method needs to extract and reconstruct the surface in each time step. In this work, this step is avoided by defining a distance estimator related to signed distance fields directly from the particle information [15].

Showcasing the validity of the model, the absorption pattern of the ray tracing scheme is compared against state-of-the-art methods; in particular, against ray-traced energy absorption patterns of laser beam welding capillaries reconstructed from x-ray imaging of different aluminum alloys [12]. Other methods include the investigation of the keyhole dynamics and absorption using welding heat-resistant glass, which allows for easy visibility of the keyhole [13]. Furthermore, one can capture the keyhole in steel welding by using a so-called sandwich specimen consisting of a sheet of stainless steel to be welded and a sheet of heat-resistant glass to be able to observe the keyhole using traditional cameras [14].

Finally, the here presented method is aimed at smoothed particle hydrodynamics simulations for which one can envision a full process simulation. Since the ray tracer interacts with the melt surface, a surface classification method is needed. There exist multiple approaches for this issue. Firstly, the so-called color field-based approach, which estimates the volume occupied in the smoothed particle hydrodynamics neighborhood of every particle [16]. Another possible criterion is visibility [17]. For example, one can determine surface particles by creating a cone in normal direction which is not occluded by the surrounding particles. A particle belongs to the surface if the cone angle exceeds a set threshold [18]. There are also other geometric criterions one can employ. For two-dimensional simulations, the radius of the circumcircle of the Delaunay triangulation yields a good indication for surface particles [19]. Opting for linear classifiers, another approach is to classify the feature space spanned by the mass-weighted average distance and the number of neighbors of each particle [20].

3 | METHOD

3.1 | Smoothed particle hydrodynamics

Smoothed particle hydrodynamics (SPH) is a Lagrangian, meshless method which discretizes the continuum by sampling points called particles representing the underlying domain [6–8]. Each aggregates a fraction of the total mass and carries quantities like velocity or density while being advected through space. A quantity A at position $\boldsymbol{x}$ is calculated by the smoothed particle hydrodynamics interpolation:

$$A(\boldsymbol{x}) = \sum\nolimits_{j \in N_x} \frac{m_j}{\rho_j} A_j W(\boldsymbol{x} - \boldsymbol{x}_j; h). \tag{1}$$

Here, the subscript denotes the affiliation of the value to the particle, that is, $A_j = A(\boldsymbol{x}_j)$. The remaining variables include the mass m, the density ρ and the kernel function W. The latter is a Gaussian-like weighting function with compact support, for which the cubic spline kernel is used [8]. Finally, h denotes the smoothing length of the kernel function and N_i the neighborhood of particles which are contained in the compact support $\bar{h} = 2h$ of i. A common approximation, is to keep the smoothing length constant over space and time. Thus, the kernel function will also be abbreviated with $W(\boldsymbol{x} - \boldsymbol{x}_j) = W(\boldsymbol{x} - \boldsymbol{x}_j; h)$ from now on.

Smoothed particle hydrodynamics also allows for the computation of spatial derivatives using the same interpolation scheme as the gradient operator:

$$\nabla A(\boldsymbol{x}) = \sum_{j \in N_x} \frac{m_j}{\rho_j} A_j \nabla W(\boldsymbol{x} - \boldsymbol{x}_j). \tag{2}$$

Likewise, one can derive the operators for divergence, curl, and the Laplacian for which the reader is kindly referred to the recent state-of-the-art report [21].

3.2 | Ray marching

Since the discretization of the fluid and heat simulation is several magnitudes coarser than the wavelength of the lasers of interest, one can safely account for its behavior by ray optics. Thus, the laser is modeled as a ray propagating from the source which linearly advances through space until it interacts with the boundary. To simulate the physical phenomena of rays, a ray tracer is employed. Particularly, this method uses a sphere tracer, which uses signed distance functions (SDF) to check for ray-boundary intersections [22]. A signed distance function $sdf(\boldsymbol{x})$ is an implicit representation of a geometry which when queried returns the signed distance to the closest point. With it, one can determine the maximum safe distance the ray can be advanced and furthermore check if it has collided with the geometry as soon as the returned distance falls under a set threshold, Figure 1.

While querying signed distance functions is rather inexpensive, explicit formulations usually have only been

Algorithm 1 A basic ray marching algorithm

Require: $x, d \in \mathbb{R}^n$ ▷ Origin and direction of ray
Require: $sdf : \mathbb{R}^n \mapsto \mathbb{R}$ ▷ Distance field (optionally signed)
Require: $\epsilon \in \mathbb{R}$ ▷ Distance threshold below which to stop marching
Require: $maxIter \in \mathbb{N}$ ▷ Maximum Iteration threshold

```
procedure MARCH(x, d, sdf; ϵ, maxIter)
    i ← 0
    while i < maxIter do
        x ← x + |sdf(x)|d
        if sdf(x) ≤ ϵ then
            return x
        end if
        i ← i + 1
    end while
    return NULL
end procedure
```

FIGURE 1 Overview over a possible ray tracing algorithm using signed distance functions.

found for rather simple geometries. For arbitrary geometries, one usually creates a signed distance field [23]. For fixed boundaries, this can be done as a preprocessing step. However, for a full process simulation, the melt pool geometry will constantly change, which would require to recompute the signed distance field in each time step. This problem can be avoided by replacing the field with a bounded distance estimator $D(\boldsymbol{x})$ which approximates the distance to the surface using the properties of smoothed particle hydrodynamics. Note that one can safely ignore the sign information by keeping track when a ray passed an interface region, since a collision-free state of all geometries is assumed.

3.2.1 | Distance estimator

For ray marching, a distance estimator is necessary to identify when a ray is colliding with an object. The quality of the distance estimator is directly tied to the efficiency of the ray tracer. Note that smoothed particle hydrodynamics does not track explicit surfaces. Since a full, explicit surface reconstruction would be computationally expensive, this method is based on the color field $c(\boldsymbol{x})$

$$c(\boldsymbol{x}) = \sum_{j \in N_x} \frac{m_j}{\rho_j} W\left(\boldsymbol{x} - \boldsymbol{x}_j\right), \tag{3}$$

which is efficiently computable solely from the existing particle information. The color field has the property to be zero outside the body's domain and smoothly transitions to one towards the inside. In fact, the color field estimates the fraction of volume occupied by smoothed particle hydrodynamics particles in the given compact support region. Thus, a color value between zero and one indicates a partially full neighborhood which commonly occurs near a free surface.

While the color field can give an indication when one is close to a free surface, the distance estimation may become inaccurate since the distance criterion is purely based on the occupied volume. For example, concave regions will always contain more particles than convex regions. Taking the gradient of the color field

$$\nabla c(\boldsymbol{x}) = \sum_{j \in N_x} \frac{m_j}{\rho_j} \nabla W\left(\boldsymbol{x} - \boldsymbol{x}_j\right) \tag{4}$$

yields a field, which is zero in fully occupied and empty regions, maximal in the transition region near the surface and indicates the direction of the surface normal $\widehat{\boldsymbol{n}} = \frac{\nabla c}{\|\nabla c\|}$. Transitioning from a position with a full neighborhood to an empty one requires at least a distance of twice the support radius, that is $2\bar{h}$, since every particle inside the starting neighborhood must be outside the neighborhood of the target position, Figure 2. Thus, it is known that in this distance of $2\bar{h}$ the color value drops from 1 to 0. Assuming the color field to drop linearly, the gradient would be a constant of $\vartheta = \frac{1}{2\bar{h}}$. Using a Gaussian-like kernel, the evolution of the color value near the free surface resembles a sigmoid function, which has a Gaussian-like gradient, Figure 2. Since the assumed linear evolution of the color field has the smallest possible maximal gradient for any continuous and differentiable function for this example, the gradient of the real color field must exceed ϑ at some point, which is used as the surface indicator. This yields the following distance estimator

$$D(\boldsymbol{x}) = \begin{cases} \left(1 - 2\bar{h}\|\nabla c(\boldsymbol{x})\|\right)\bar{h}, & \text{if } \|\nabla c(\boldsymbol{x})\| < \vartheta = \frac{1}{2\bar{h}} \\ 0, & \text{otherwise} \end{cases}. \tag{5}$$

Since the distance estimator is reliant on the neighborhood, the compact support radius $\bar{h}$ dictates an upper bound for the maximum distance the ray tracer is allowed to take.

3.3 | Laser beam model

In the model, the laser is represented as a bundle of idealized light rays following the optics of electromagnetic waves. These include the effects of absorption, attenuation, reflection, and refraction. In the following, the models for capturing the afore mentioned effects are presented.

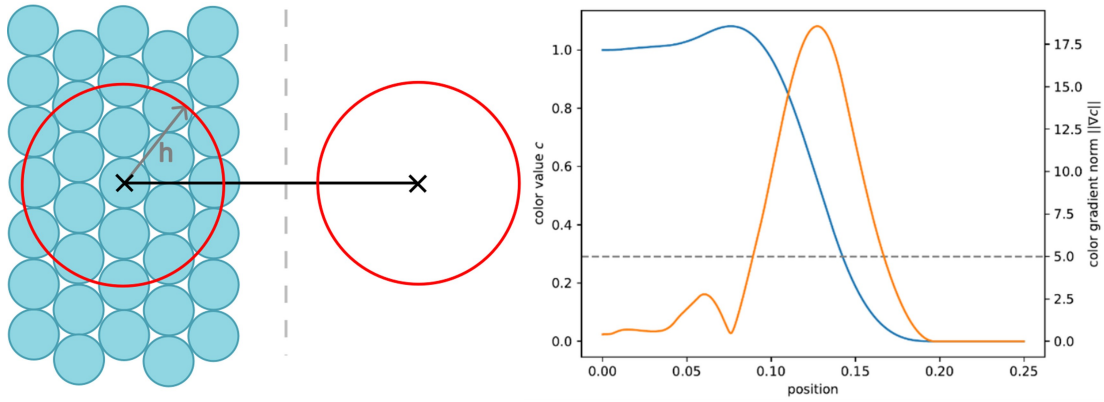

FIGURE 2 a) Schematic representation of the neighborhood information near the free surface. The implicit surface used by the ray tracing method is indicated by the dashed line. b) Plot of the color field (blue) and norm of the color gradient (orange) perpendicular to the surface along the line in 2a). The dashed line represents the cut-off value of of $||\nabla c||$, that is $\vartheta = \frac{1}{2\bar{h}}$.

3.3.1 | Absorption and attenuation

While passing through an optical medium, fractions of the ray's energy is absorbed by the material. The amount of absorbed energy is exponentially dependent on the depth of the transmission and the material and wavelength specific attenuation coefficient μ. Their relation is given by the Beer-Lambert law

$$\Delta\Phi_e^{att}(\Delta x) = \Phi_e e^{-\mu\Delta x}, \tag{6}$$

where Φ_e denotes the radiant flux and Δx the distance inside the optical medium.

The attenuated energy of the ray is modeled as heat absorbed by the material. The absorbed radiant flux Q is distributed around the position $\boldsymbol{x}$ to the surrounding particles using an inverse distance weighting function

$$\left(\frac{dQ}{dt}\right)_i = \frac{\Delta\Phi_e^{att} W(\boldsymbol{x} - \boldsymbol{x}_i)}{\sum_{j\in N_x} W(\boldsymbol{x} - \boldsymbol{x}_j)}. \tag{7}$$

Integrating the Beer-Lambert law into the ray marching scheme, the linearized attenuation is calculated for each step taken and the rays' power is updated accordingly

$$\Phi_e(x + \Delta x) = \Phi_e(x) - \Delta\Phi_e^{att}(\Delta x). \tag{8}$$

Additionally, the advancements of the ray marching scheme inside any medium is limited to $\frac{1}{4}\bar{h}$ to guarantee a smooth distribution of the absorbed power.

Finally, one can model complete surface absorption by setting the attenuation coefficient as one. Thus, any non-reflected ray gets fully absorbed by the first layer of particles.

3.3.2 | Reflection

This work assumes that any reflection is purely based on specular reflections, that is, an incoming ray is reflected at the same angle to the surface normal as its incident angle. Note that most of the materials of interest in the field of laser beam welding, like aluminum or steel, can be classified as dominantly specular, supporting the choice. Given the properties of the reflection, the incoming, normalized ray direction $\widehat{\boldsymbol{d}}_i$, and the surface normal $\widehat{\boldsymbol{n}}$, the reflected, normalized direction vector of the ray $\widehat{\boldsymbol{d}}_{refl.}$ can be determined by

$$\widehat{\boldsymbol{d}}_{refl.} = \widehat{\boldsymbol{d}}_i - 2\left(\widehat{\boldsymbol{d}}_i \cdot \widehat{\boldsymbol{n}}\right)\widehat{\boldsymbol{n}}. \tag{9}$$

3.3.3 | Refraction

When a light ray passes from one optical medium to another, it not only gets reflected, but also part of it gets refracted inside the optical medium. The direction of the transmitted ray is based on the associated phase velocities. Its behavior can be modeled by Snell's law

$$\frac{\sin\theta_1}{\sin\theta_2} = \frac{n_2}{n_1}, \tag{10}$$

where θ is the incident angle between the surface normal and the rays, n the refractive index and the subscripts denote the affiliation to the optical medium. The normalized direction vector of the refracted ray $\widehat{\boldsymbol{d}}_{refr.}$ can be derived from Snell's law which yields

$$\widehat{\boldsymbol{d}}_{refr.} = \sqrt{1 - n_{12}^2\left[1 - \left(\widehat{\boldsymbol{d}}_i \cdot \widehat{\boldsymbol{n}}\right)^2\right]}\widehat{\boldsymbol{n}} + \mathrm{n}_{12}\left[\widehat{\boldsymbol{d}}_i - \left(\widehat{\boldsymbol{d}}_i \cdot \widehat{\boldsymbol{n}}\right)\widehat{\boldsymbol{n}}\right], \tag{11}$$

where $n_{12} = n_1/n_2$ is the ratio of refractive indices. Note that $\widehat{\boldsymbol{d}}_{refr.}$ is defined if the critical angle given by Snell's Law is not reached, that is

$$\theta_1 < \theta_{crit.} = \sin^{-1}(n_{12}). \tag{12}$$

Otherwise, the ray experiences total internal reflection which can be modeled by specular reflections.

Usually at an interface, both processes of reflection and refraction take place. Thus, the total radiant flux of the incoming ray will be split between the reflected and the refracted one. The reflectance R denotes the ratio between incoming and reflected power and is dependent on the incidence angle θ_1. For the ray tracer, Schlick's approximation is used

$$R(\theta_1) = R_0 + (1 - R_0)(1 - \cos\theta_1)^5 \tag{13}$$

$$R_0(n_1, n_2) = \left(\frac{n_1 - n_2}{n_1 + n_2}\right)^2,\ R_0(\underline{n}_1, \underline{n}_2) = \left|\frac{\underline{n}_1 - \underline{n}_2}{\underline{n}_1 + \underline{n}_2}\right|^2, \tag{14}$$

where R_0 is the reflectance under an incidence angle of zero and $\underline{n}$ the complex refractive index [24]. Accordingly, the transmittance T refers to the ratio between incoming and transmitted and refracted power

$$T = 1 - R. \tag{15}$$

The power of the reflected ray Φ_e^R and the refracted ray Φ_e^T can thus be calculated from the power of the incoming ray Φ_e by using

$$\Phi_e^R = R\Phi_e,\ \Phi_e^T = T\Phi_e,\ \Phi_\mathrm{e} = \Phi_e^R + \Phi_e^T. \tag{16}$$

3.3.4 | Laser model

It is assumed that the laser consists of Gaussian beams. Since even spatially coherent lasers experience some spread, the laser's light emission is modeled as a narrow cone with a focal point F, a beam waist w_0 at its focal point and the Rayleigh length z_R at which the cross-sectional area of the beam doubles, Figure 3. The direction of each light ray from the laser is determined by the vector from the origin of the cone to a quasi-randomly sampled point on the focal disk. For sampling, a Halton sequence instead of a completely random distribution is employed to achieve a better coverage of all possible beam angles. This returns samples inside the domain $[-1,\ 1]^2$ from which every sample outside the unit disk is discarded and the resulting points are transformed to the focal disk. Depending on the sample position, one can assign different power values to the rays for modelling, for example a Gaussian or a top hat laser with a uniform distribution.

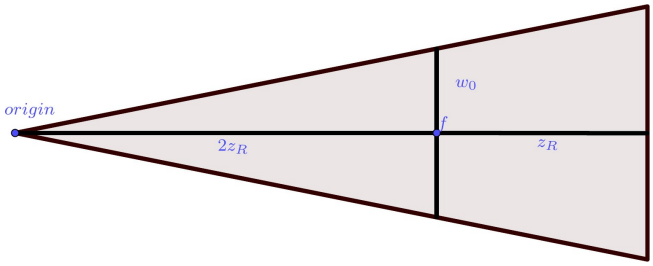

FIGURE 3 Schematic representation of a Gaussian laser beam. w_0 denotes the beam waist at the focal point f and z_R the Rayleigh length.

4 | RESULTS

The presented method is implemented using SPlisHSPlasH, an open-source smoothed particle hydrodynamics computational fluid dynamics library [21]. This includes having direct access to the neighborhood search needed for an efficient evaluation of the ray tracer. Additionally, since SPlisHSPlasH has already been used in the process simulations of tungsten inert gas welding (TIG) and thermal spraying, the temperature and fluid simulation can be leveraged for a full process simulation in future [9–11].

4.1 | Laser beam ray tracing

The ray tracer is validated by investigating the resulting behavior of the rays in different test scenarios corresponding to the considered effects in isolation. Thus, the light paths and total absorbed energy in the test cases of reflection, refraction, and attenuation are examined. For the simulations, 10000 initial rays with 10 reflections and refractions each are used which in turn can split into two rays each through their interface behavior. In all experiments, the number of rays has never exceeded 100000 rays. Lastly, a cubically shaped laser beam bundle with a Gaussian power distribution and a total power of 100 W is used for the tests.

4.1.1 | Reflection

In this test, the reflection and absorption behavior is investigated. The first test consists of a simple reflection of a laser beam under a 45° angle without any refraction and attenuation. Furthermore, a reflectance of $R = 0.5$ is used and any not-reflected power is directly absorbed by the material as heat.

The results show the expected behavior, Figure 4. The outgoing rays are reflected under the same 45° angle to the surface normal as the incoming rays. Furthermore, the total absorbed wattage is half of the total wattage, indicating that reflectance is modeled correctly. Lastly, since the model uses the smoothed particle hydrodynamics kernel function to distribute the absorbed power, the absorption pattern is smooth and reflects the input energy profile of the laser.

Next, more challenging geometries are investigated with rays entering a fully specular cup shaped object.

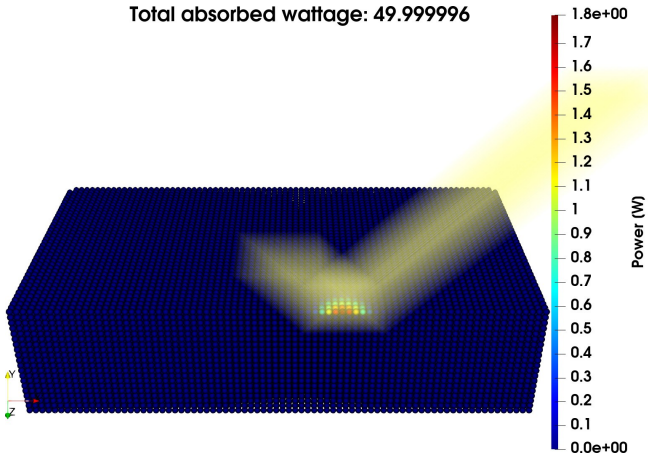

FIGURE 4 Surface power absorption in case of specular reflection of 10000 rays with a Gaussian power distribution with a total input power of $P = 100$ W and $R = 0.5$, $\mu = 1$.

The laser enters the shape at an 11.3° angle. Furthermore, the reflectance is set to $R = 0.5$, thus half of the power of each ray is absorbed each time the ray reflects off the cup.

The resulting light rays are mostly reflected in the correct direction and showcase the expected behavior, Figure 5. However, near the entry edge of the cup, some light rays are reflected at a slightly erroneous angle. This behavior can be deduced to the surface normal calculation using smoothed particle hydrodynamics. Since the normals are computed as the smoothed interpolation of the color gradient field, sharp features of the boundary model will get smoothed, thus creating rounded edges over the cup. Still, only a minor fraction of the incoming rays is reflected at an erroneous angle leading only slight errors in the final energy distribution.

In terms of absorbed energy, the ray tracing approach yields a wattage of 69 W, Figure 5. In comparison, a simple projection-based approach does not directly handle the internal reflections inside the cup and thus reports an absorbed wattage of 50 W. Since the ray tracing approach considers multiple reflections, the energy distribution as well as the total absorbed wattage are better captured.

Furthermore, the reflectance and thus the absorbed energy can also be computed using Schlick's approximation. A synthetic scenario has been simulated where a work piece with varying refractive indices n_2 has been subjected to a bundle of rays approaching at an 45° angle of incidence. The surrounding air has a refractive index of $n_1 = 1$. The results show the expected behavior that higher refractive indices yield a higher reflectance and thus a lower energy absorption, Figure 6.

Lastly, the transition from partial to total reflection is considered. Thus, the synthetic scenario is being simulated with the refractive indices of the surrounding space and the workpiece being $n_1 = \sqrt{2}$ and $n_2 = 1$. This yields

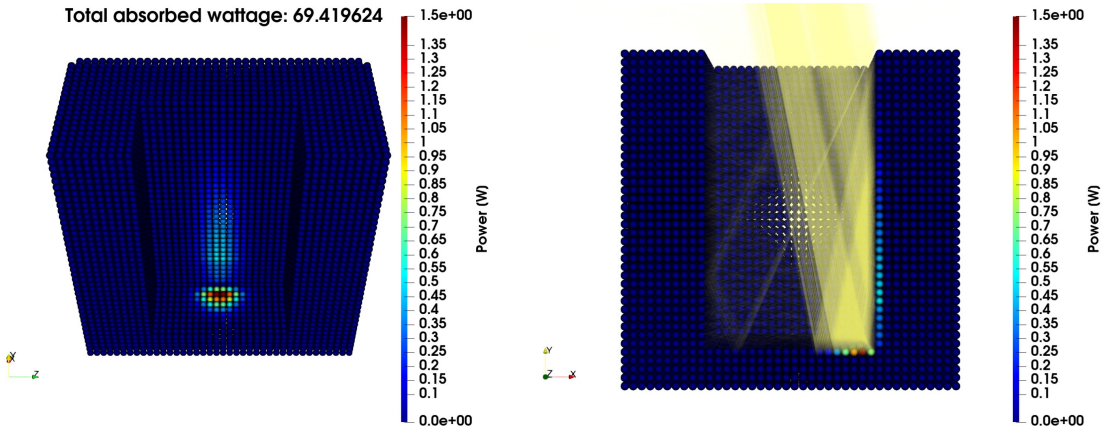

FIGURE 5 Surface power absorption for a cup shaped geometry using 10000 rays with a Gaussian power distribution with a total input power of $P = 100$ W and $R = 0.5$, $\mu = 1$.

a critical angle of $\theta_{crit.} = 45°$. Below this angle, rays will be transmitted and reflected given by the transmittance and reflectance of the material, Figure 7. Above this angle, the full set of rays will be reflected through total reflection, Figure 8.

4.1.2 | Refraction

Next, the refraction behavior is analyzed. Thus, rays are passed through a 1 m thick pool of water ($n_2 = 1.33$, $\mu(500\ nm) = 0.06\ m^{-1}$) sampled with particles. For the surrounding void regions, $n_1 = 1$ is assumed. The results are visually conforming with the expected results at the two interfaces with incidence angles θ_1, θ_2 at the first and θ_2, θ_3 at the second interface. The observed refraction angles are $\theta_2 \approx 32°$, $\theta_1 = \theta_3 \approx 45°$ of the whole bundle of rays, Figure 9. Single rays can slightly deviate from their expected refraction vector due to numerical errors in the normal computation. However, these errors have a negligible impact on the resulting energy distribution and shape of the beam.

4.1.3 | Excursus: Attenuation

While in practice, the layer in which the absorption takes place in laser beam welding with typical wavelengths of $\lambda \in [500,\ 1000]$ nm can be assumed to be the surface, the presented method can also simulate the correct attenuation behavior for transparent media.

For attenuation, a synthetic scenario of the laser passing a 1 m thick domain with an attenuation coefficient of $\mu = 0.5\ \mathrm{m}^{-1}$ is investigated. Reflection is ignored by setting the reflectance and transmittance to $R = 0,\ T = 1$. Thus, the absorbed wattage and energy distribution is entirely comprised of the absorption through attenuation. From the results, a good agreement can be found with the 50 W absorption target, attributing the small error to numerical issues, Figure 10.

Furthermore, another scenario has been investigated in which the penetration depth of a single light ray has been considered. The same values for reflectance and transmittance have been chosen as in the previous scenario and the attenuation coefficient has been swept in the range of $\mu \in [0,\ 4.5]\ \mathrm{m}^{-1}$. Modelling attenuation

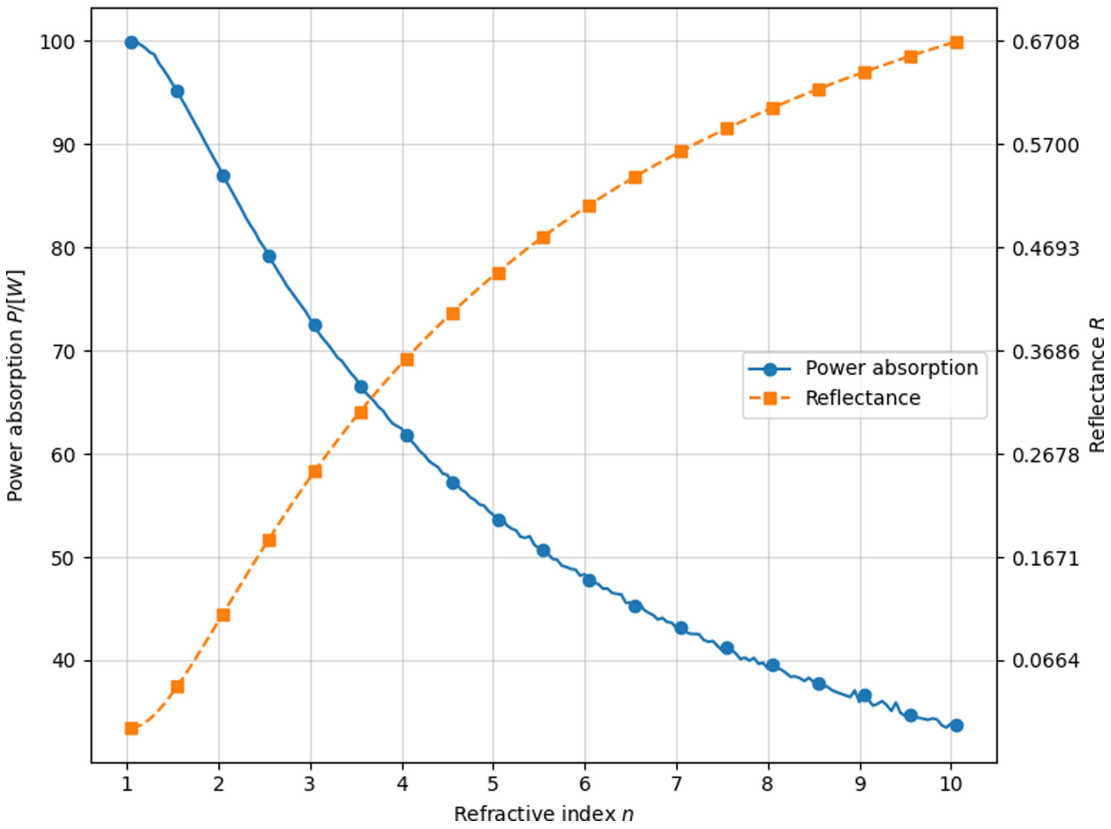

FIGURE 6 Plot of reflectance and absorbed power against refractive index with an angle of incidence $\theta = 45°$. Reflectance has been modeled after Schlick's approximation, which approximates the results of the Fresnel equations. Thus, the expected behavior of an increase in reflectance and thus a decrease in absorbed power can be observed when increasing the refractive index.

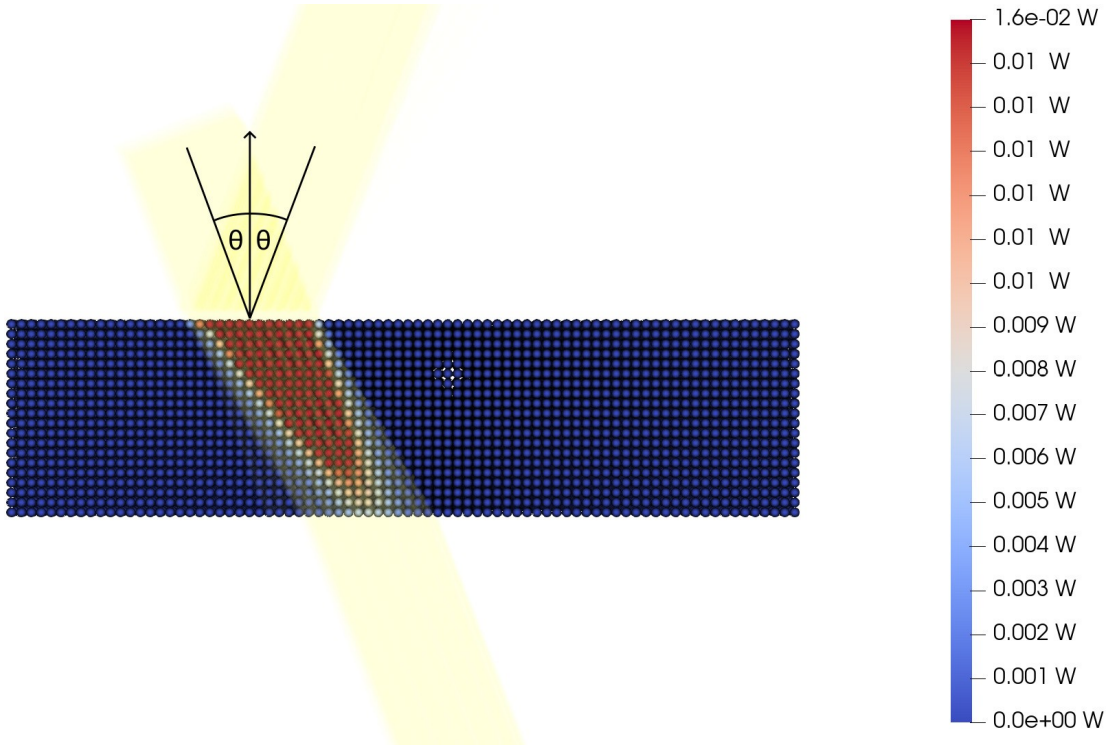

FIGURE 7 Refraction of a single laser beam as a bundle of light rays happening in a synthetic scenario. The environment and work piece have a refractive index of $n_1 = \sqrt{2}$ and $n_2 = 1$, respectively. Thus, the first refraction can become subject to total reflection. Since the angle of incidence $\theta_1 \approx 22^\circ$ at the first interface is below the critical angle of $\theta_{crit.} = 45^\circ$, the expected behavior of partial reflection can be observed. Any rays with more than two reflections have been discarded for visual clearance. The color mapped particles show the absorption of the transmitted rays happening inside the workpiece.

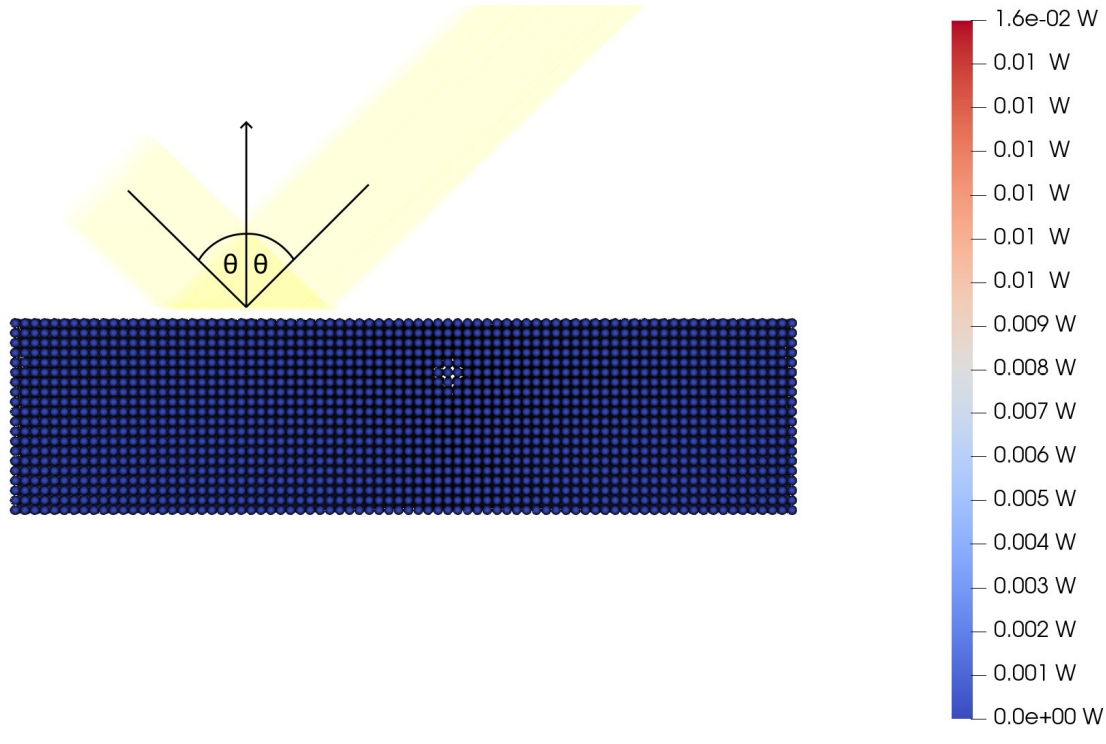

FIGURE 8 Total reflection happening at an incidence angle of $\theta = 45^\circ$. The scene has the same parameters as in the partial reflection example, Figure 7.

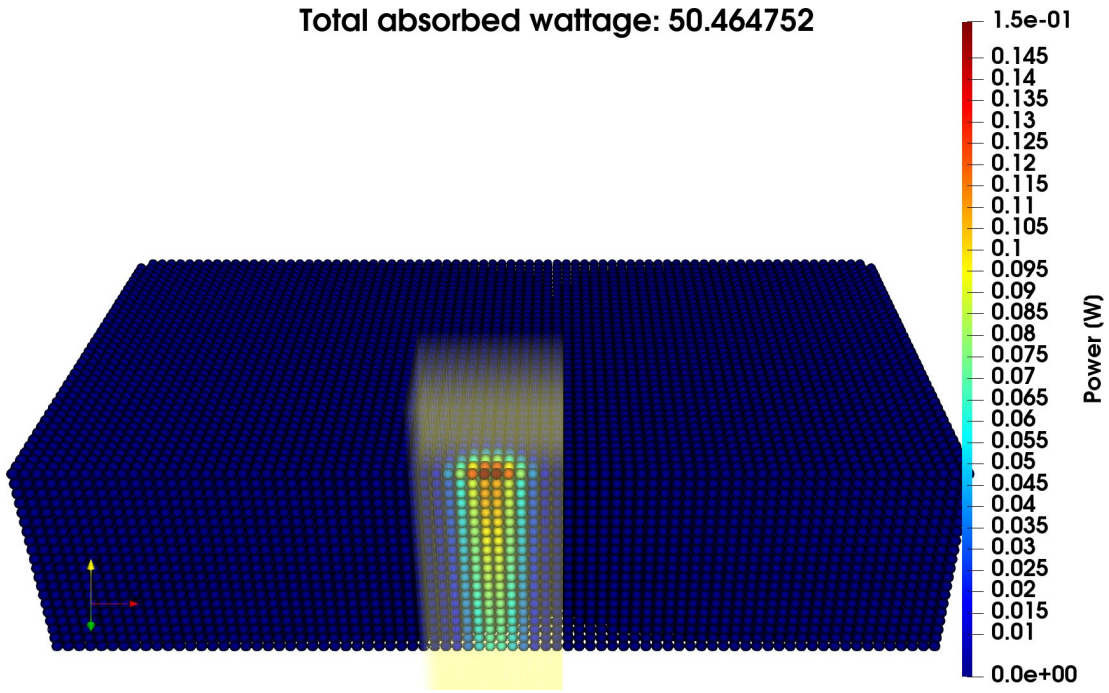

FIGURE 9 Volumetric power absorption inside a $1m$ thick work piece with 10000 rays with a Gaussian power distribution with a total input power of $P = 100$ W and $R = 0.0$, $\mu = 0.5$ m^{-1}.

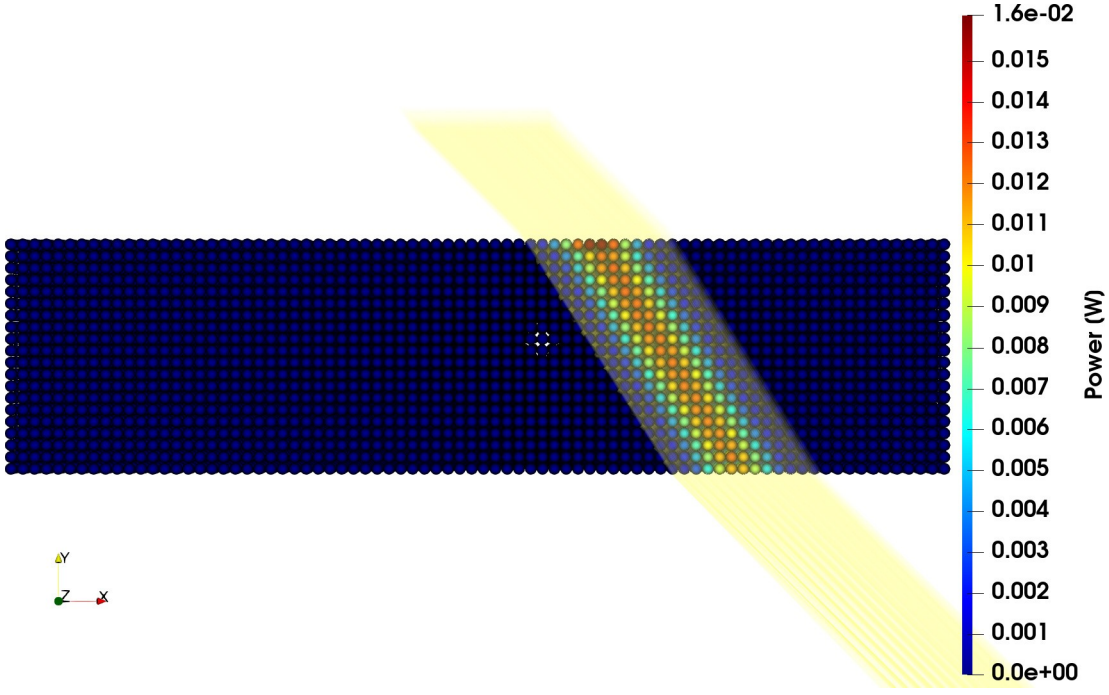

FIGURE 10 Refraction and Attenuation of rays passing through a block of water. The refractive indices of the environment and of water are $n_1 = 1$ and $n_2 = 1.33$, respectively.

using the Beer-Lambert law, any light ray may only lose all its power at an infinite penetration depth. Thus, it is advisable to set a cut-off value at which it is considerable that the ray's energy got fully absorbed through attenuation. In this test, a cut-off value of $P_{\text{cutoff}} = 10^{-8}$ W is used. One can also compute the analytical maximum penetration depth given Beer-Lambert's law. Although the attenuation - and thus also the

maximum penetration depth - is computed in discrete steps, the simulated and analytical results show a strong agreement, Figure 11.

4.1.4 | Focus

Recall that the laser is modeled as a cone of rays. Thus, investigating whether the typical behavior of a laser with hyperbolic spread can be captured is the goal of the following scenario by placing a work piece with a step inside the cone of the laser. The upper part of the work piece has a distance of 1 m to the lower part, which is chosen to be the Rayleigh length of the laser. Its source distribution is a top hat laser and positioned in a way, that the upper spot radius is 0.5 m.

Thus, the lower spot radius is expected to be 1 m, which is what is being observed, Figure 12. Furthermore, the presented model is compliant with the inverse square law, since the spatial average absorbed power of the lower spot is exactly a quarter of the one of the upper part. However, some artifacts of the energy distribution are noticeable at the edge of the workpiece. These can be attributed to the renormalization of the absorbed heat energy, which is necessary for energy conservation in transferring the energy from the beam to the particles.

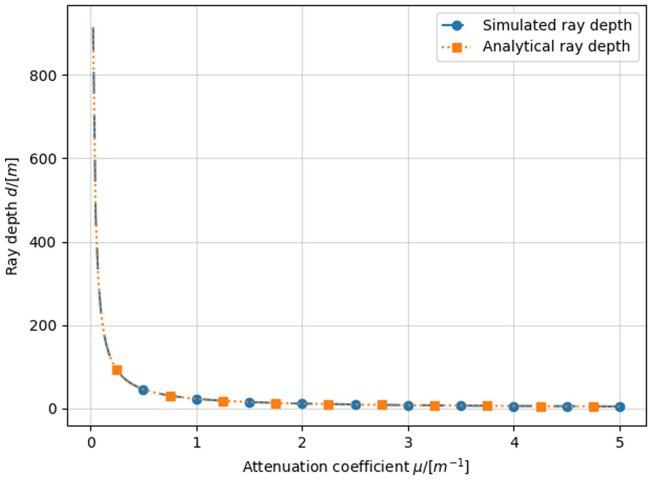

FIGURE 11 Comparison of analytical and simulated results for penetration depth of a laser beam with varying attenuation coefficients $\mu \in [0,\ 4.5]\ m^{-1}$ using the Beer-Lambert law. The maximum deviation of both results is at most 1 %.

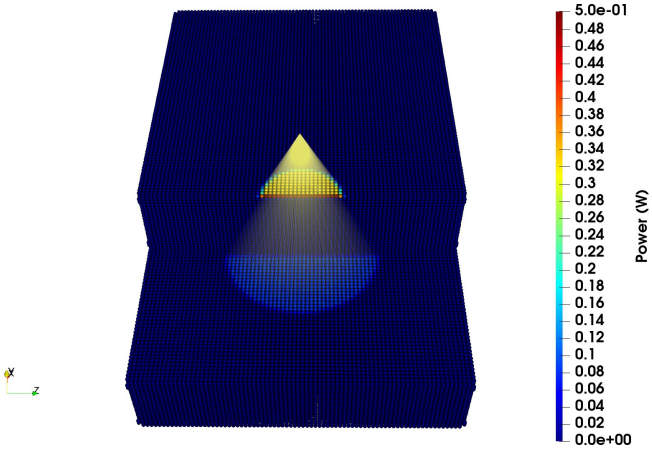

FIGURE 12 Focus and spread of the laser beam model where the section closer to the laser's origin lies in the focus. The lower section is placed a Rayleigh length $z_R = 0.5$ m further away from the origin and the beam has a waist of $w_0 = 0.5$ m.

4.2 | Laser beam welding

Demonstrating the validity and capabilities of the ray tracer, the energy distribution inside a real-world scenario shall also be investigated. In particular, the absorbed energy inside capillaries formed by laser beam welding of the aluminum alloy AA1050 A (Al99.5) are compared [12], Figure 13. The reconstructed surface is a triangle mesh of the formed capillaries from x-ray images. The absorbed irradiance E_{absorbed} [W/mm^2] of the state-of-the-art results inside the closed and open capillary was determined with a total input power of $P = 1$ kW and $P = 1.2$ kW, respectively, using ray tracing with a maximum of 150000 randomly polarized rays reflecting inside the cavity.

The comparison was performed with the same parameters. For efficiency reasons, only specular reflections are considered, which are the dominant behavior of the investigated materials and wavelengths. Thus, the capillary is placed inside a surrounding domain and

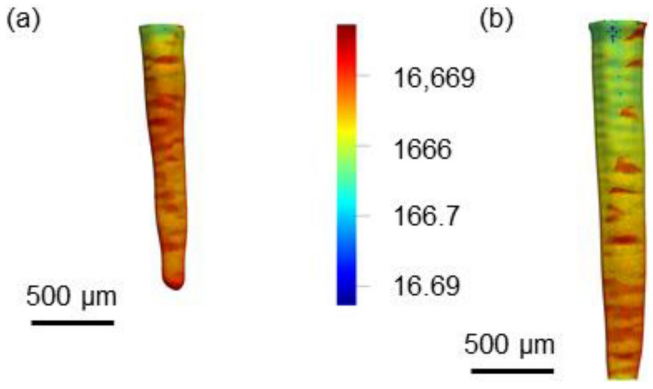

FIGURE 13 Distribution of the simulated, locally absorbed irradiance E_{absorbed} [W/mm^2] inside the reconstructed capillaries [12]. (a) Full-penetration welding in mode A with $P = 1$ kW. (b) Full-penetration welding in mode B with $P = 1.2$ kW. Reproduced with permission [12].

the resulting geometry is sampled using a smoothed particle hydrodynamics-based volume sampling [25]. As the method could also handle volumetric effects, the attenuation has been set to fully absorb any transmitted ray instantly. Comparing the results, a striking resemblance can be found in the energy distribution between the presented method and the state of the art [12], Figure 14. The distinct horizontal bands with high absorption have been observed, as well as a general increase in absorption deeper into the capillary. Both methods also agree qualitatively. Assuming that most of the absorption happens inside the topmost layer of particles, one can convert the reported power density into an irradiance. Since the surface possesses a thickness of a particle diameter, i.e. $d_{\text{particle}} = 4 \cdot 10^{-6}$ m, the irradiance E can be transformed into a volumetric power density $\mathcal{P}$

$$\mathcal{P} = E/d_{\text{particle}}. \tag{17}$$

Transforming the upper end of the irradiance bar into a volumetric power density yields $\mathcal{P}\left(1.6 \cdot 10^4 \frac{\text{W}}{\text{mm}^2}\right) = 4 \cdot 10^{15} \frac{\text{W}}{\text{mm}^3}$, which is in the same order of magnitude as the results of the employed ray tracing method.

Thus, the ray tracer produces comparable results with state-of-the-art methods.

5 | CONCLUSIONS AND FUTURE WORK

This work demonstrates that the ray tracing problem, a global surface-based effect, can be handled efficiently in smoothed particle hydrodynamics. Relying on explicit surface representations, for example through surface tracking or reconstruction, typically results in losing many of the attractive features the locality of smoothed particle hydrodynamics entails, such as good performance and simple formulation of effects. A native smoothed particle hydrodynamics surface handling approach based on signed distance fields has been introduced that retains the attractive features of the smoothed particle hydrodynamics paradigm. The quality of the results obtained from the ray tracer is very promising, as can be seen in the comparison against state-of-the-art results. Thus, further investigations of the surface handling approach for other problems remains an interesting topic. Furthermore, this work forms an important segment of multi-physics process simulations incorporating fluid, melt and laser dynamics for laser welding. The most relevant remaining section consists of the development of a recoil pressure model to model the pressure forces resulting from the evaporation of material. Since this is also a surface-based effect, there is potential reusing the presented surface handling in whole or in parts.

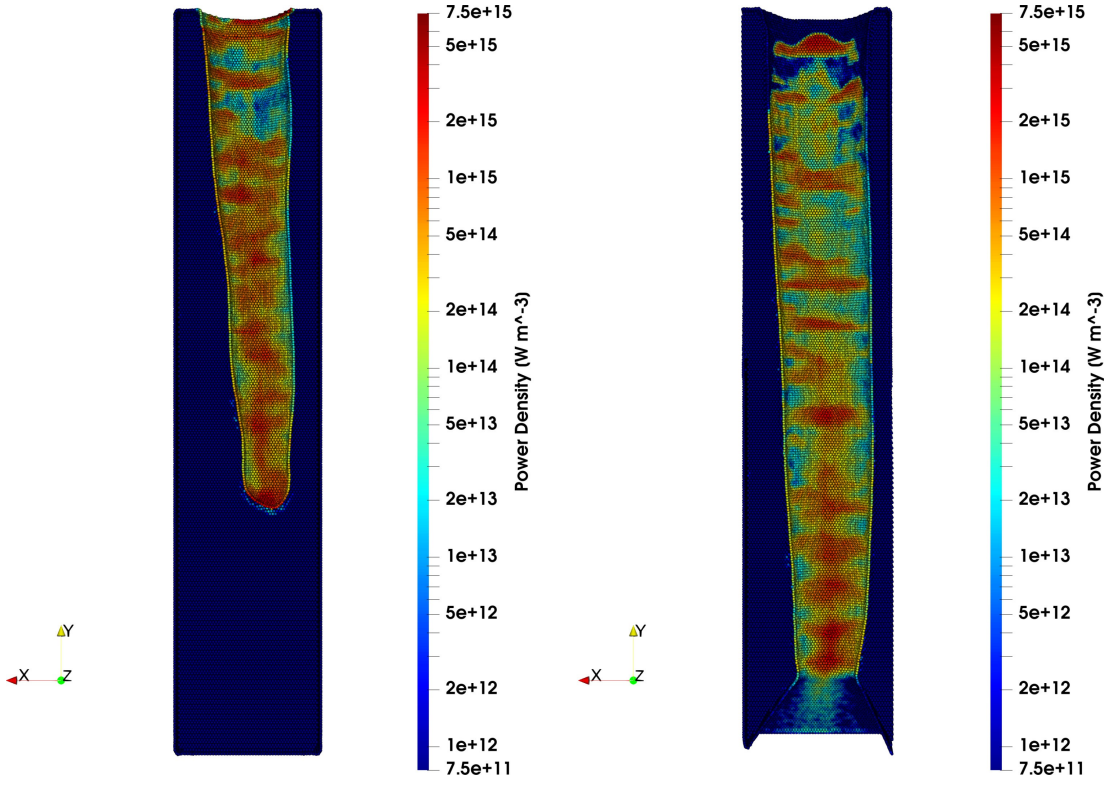

FIGURE 14 Distribution of the simulated, absorbed power density inside the reconstructed capillaries with $P = 1$ kW and $P = 1.2$ kW, respectively.

Furthermore, a thorough investigation of the performance remains an open task. The preliminary results are promising, since the approach was able to handle problems of significant complexity (simulations of around 700k particles, and up to 100k rays). In a full process simulation, the number of evaluations would be larger by several orders of magnitude. However, due to the considerations in terms of efficiency, it can be argued that the presented method should be suited for these use cases.

Lastly, process simulations exhibit strong temporal relations between two timesteps. Currently, this is not considered in the surface representation and its inclusion could provide significant performance improvements.

ACKNOWLEDGEMENTS

The presented investigations were carried out at RWTH Aachen University within the framework of the Collaborative Research Centre SFB1120-236616214 "Bauteilpräzision durch Beherrschung von Schmelze und Erstarrung in Produktionsprozessen" and funded by the Deutsche Forschungsgemeinschaft e. V. (DFG, German Research Foundation). The sponsorship and support is gratefully acknowledged. J. Kruska and L. Westhofen contributed equally to the presented work. Open access funding enabled and organized by Projekt DEAL.

ORCID

L. Westhofen http://orcid.org/0000-0003-4427-2377
S. Warkentin http://orcid.org/0009-0004-4514-8962
R. Sharma http://orcid.org/0000-0002-6976-4530
U. Reisgen http://orcid.org/0000-0003-4920-2351

REFERENCES

1. D. Sollich, E.-N. Reinheimer, J. Wagner, P. Berger, P. Eberhard, *J. Theor. Appl. Mech.* **2022**, *96*, 26.
2. A. Otto, H. Koch, R. G. Vazquez, *Phys. Procedia.* **2012**, *39*, 843.
3. H. Hu, F. Fetzer, P. Berger, P. Eberhard, *GAMM.* **2016**, *39*, 149.
4. H. Hu, F. Fetzer, P. Berger, P. Eberhard, *PARTICLES* **2017**, *84*, 450.
5. M. Courtois, M. Carin, P. Le Masson, S. Gaied, M. Balabane, *J. Phys. D* **2013**, *46*, 505305.
6. R. a Gingold, J. J. Monaghan, *Mon. Not. R. Astron. Soc.* **1977**, 375.
7. J. J. Monaghan, *Annu. Rev. Astron. Astrophys.* **1992**, *30*, 543.
8. J. J. Monaghan, *Rep. Prog. Phys.* **2005**, *68*, 1703.
9. K. Bobzin, H. Heinemann, K. Jasutyn, S. R. Jeske, J. Bender, S. Warkentin, O. Mokrov, R. Sharma, U. Reisgen, *J. Therm. Spray Technol.* **2023**, *32*, 599.
10. S. R. Jeske, J. Bender, K. Bobzin, H. Heinemann, K. Jasutyn, M. Simon, O. Mokrov, R. Sharma, U. Reisgen, *Comp. Part. Mech.* **2022**, *9*, 1137.
11. S. R. Jeske, M. S. Simon, O. Semenov, J. Kruska, O. Mokrov, R. Sharma, U. Reisgen, J. Bender, *Comp. Part. Mech.* **2022**, *10*, 1.
12. J. Wagner, C. Hagenlocher, M. Hummel, A. Olowinsky, R. Weber, T. Graf, *Metals.* **2021**, *11*, 797.
13. X. Jin, P. Berger, T. Graf, *J. Phys. D* **2006**, *39*, 030.
14. M. Zhang, G. Chen, Y. Zhou, S. Li, *Opt. Express.* **2013**, *21*, 19997.
15. M. W. Jones, J. A. Baerentzen, M. Sramek, *TVCG.* **2006**, *12*, 581.
16. M. Müller, D. Charypar, M. Gross, *SCA.* **2003**, 154.
17. M. Sandim, D. Cedrim, L. G. Nonato, P. Pagliosa, A. Paiva, *CGF.* **2016**, *35*, 215.
18. A. Barecasco, H. Terissa, C. F. Naa, *Comp. Phys.* **2013**.
19. Y. Lin, G. R. Liu, G. Wang, *J. Comput. Phys.* **2019**, *383*, 196.
20. F. Zorrilla, J. Sappl, W. Rauch, M. Harders, *Computers.* **2019**.
21. D. Koschier, J. Bender, B. Solenthaler, M. Teschner, *EUROGRAPHICS* **2019**.
22. J. C. Hart, *Vis. Comput.* **1996**, *12*, 527.
23. D. Koschier, C. Deul, J. Bender, *SCA* **2016**, pp. 1.
24. C. Schlick, *CGF.* **1994**, *13*, 233.
25. T. Kugelstadt, J. Bender, J. A. Fernández-Fernández, S. R. Jeske, F. Löschner, A. Longva, *Proc. ACM Comput. Graph. Interact. Tech.* **2021**, *4*.

How to cite this article: L. Westhofen, J. Kruska, J. Bender, S. Warkentin, O. Mokrov, R. Sharma, U. Reisgen, *Materialwiss. Werkstofftech.* **2024**, *55*, e202300161. https://doi.org/10.1002/mawe.202300161